Waveguide-integrated, plasmonic enhanced graphene photodetectors

Jakob E. Muench,[†] Alfonso Ruocco,[†] Marco A. Giambra,[‡] Vaidotas Miseikis,[‡,¶,§] Dengke Zhang,[†] Junjia Wang,[†] Hannah F.Y. Watson,[†] Gyeong C. Park,[†] Shahab Akhavan,[†] Vito Sorianello,[†] Michele Midrio,[‖] Andrea Tomadin,[⊥] Camilla Coletti,[¶,§] Andrea C. Ferrari,[*,†] and Ilya Goykhman[#]

†*Cambridge Graphene Centre, University of Cambridge, Cambridge CB3 0FA, UK*

‡*Consorzio Nazionale per le Telecomunicazioni, 56124 Pisa, Italy*

¶*Center for Nanotechnology Innovation @ NEST, Istituto Italiano di Tecnologia, 56127 Pisa, Italy*

§*Graphene Labs, Istituto Italiano di Tecnologia, 16163 Genova, Italy*

‖*Consorzio Nazionale per le Telecomunicazioni, University of Udine, 33100 Udine, Italy*

⊥*Dipartimento di Fisica, Università di Pisa, Largo Bruno Pontecorvo 3, 56127 Pisa, Italy*

#*Micro- and Nanoelectronics Center, Technion, Haifa 320000, Israel*

E-mail: acf26@eng.cam.ac.uk

Abstract

We present a micrometer scale, on-chip integrated, plasmonic enhanced graphene photodetector (GPD) for telecom wavelengths operating at zero dark current. The GPD is designed to directly generate a photovoltage by the photo-thermoelectric effect, is made of chemical vapor deposited single layer graphene, and has an external responsivity∼12.2V/W with a 3dB bandwidth∼42GHz. We utilize Au split-gates to

electrostatically create a p-n-junction and simultaneously guide a surface plasmon polariton gap-mode. This increases light-graphene interaction and optical absorption and results in an increased electronic temperature and steeper temperature gradient across the GPD channel. This paves the way to compact, on-chip integrated, power-efficient graphene based photodetectors for receivers in tele and datacom modules.

Keywords

graphene, photodetector, photo-thermoelectric effect, integrated photonics, plasmonics

The ever-growing demand for global data traffic[1] is driving the development of next generation communication standards.[2–4] The increasing numbers of connected devices,[5] the need for new functionalities, and the development of high-performance computing[6,7] require optical communication systems and their key building blocks (photodetectors (PD), modulators, ...) to perform at higher speeds, with improved energy-efficiency, whilst maintaining scalability and cost-effective manufacturing. Si photonics[8,9] enables dense (nanoscale) integration[10] relying on mature, low-cost (based on complementary metal-oxide-semiconductor (CMOS) fabrication processes) manufacturing,[8,9] making it one of the key technologies for short-reach (<10km) optical interconnects[7,11] beyond currently employed $LiNbO_3$[12,13] and InP.[14,15]

Si photonics based receivers, where the optical-to-electrical signal conversion is performed, typically employ Ge[16] or bonded III-V PDs,[17,18] since the photon energies at telecom wavelengths (λ =1.3-1.6μm) are not sufficient for direct (band-to-band) photodetection in Si.[19] In particular, on-chip integrated Ge PDs[20–24] have matured into standard components in Si photonics foundries[8,9,19] and nowadays perform close to their physical limits.[8] Their external responsivities (in A/W), $R_I = I_{\rm ph}/P_{\rm in}$, where $I_{\rm ph}$ is the photocurrent and $P_{\rm in}$ is the incident optical power, can exceed 1A/W[8,20] and their bandwidth can reach 60-100 GHz[22–25] for speed-optimised designs. Following the development of high temperature ($> 600°$C)[16]

heterogeneous integration of Ge-on-Si using epitaxial growth and cyclic thermal annealing,[16,26,27] the concentration of defects and threading dislocations in Ge epilayers and at Si/Ge interfaces can be reduced,[16] resulting in low (<10nA[9,24]) dark current in waveguide integrated Ge p-i-n photodiodes.[21,24] However, Ge-on-Si integration is complex,[16,19,27] as the lattice mismatch between Si and Ge,[16] ion implantation,[20,22] thermal budget (i.e. thermal energy transfer to the wafer) management,[19] and the non-planarity of Ge layers[27] require dedicated solutions during device fabrication.[9] The charge carrier mobility μ in Si and the dislocations and defects in grown[16] or evaporated[28] Ge layers set intrinsic limits that prevent further improvements to the operation speed of Ge PDs without compromising R_I.[9,23] These shortcomings, together with the spectrally limited operation regime (band edge in Ge$\sim$ 1.57μm,[19] which can be extended to$\sim$ 1.62μm[29] at the expense of R_I), and the incompatibility of Ge epitaxy for monolithic integration with other material platforms, such as SiN, are limitations for Ge PDs.[8,30] Thus, novel solutions for PDs, integrated with Si photonics, at telecom bands are needed.

Graphene is a promising candidate for on-chip integrated photonics.[31–54] The advantages of single-layer graphene (SLG) stem from its superior optoelectronic properties.[55] These include high-speed (>200GHz,[56] calculated from the impulse response time in a vertically illuminated metal-graphene-metal structure) operation,[57] broadband (ultraviolet to far-infrared) absorption,[58–60] efficient optical modulation (electro-optical index change $\Delta n_{\text{eff}} > 10^{-3}$),[31–38] CMOS compatibility[41,61] and integrability[31,62,63] with different on-chip photonics platforms, such as silicon-on-insulator (SOI)[32] and SiN.[35] In the case of waveguide-integrated graphene PDs (GPDs),[40–54] high speeds up to 128GHz,[49] wafer-scale integration[48] and R_I $\sim$0.4-0.5A/W[43,47,50,51] were reported. GPDs can offer broadband detection across multiple telecommunication channels (O-band$\sim$1.31μm to U-band$\sim$1.65μm),[41] bias-free operation,[64] and direct generation of photovoltage.[45,64] The latter opens up the possibility of building GPDs without the noise contribution of dark current[31,46] and eliminates the need of noise-prone trans-impedance amplifier (TIA) to convert current-to-voltage in the read-out

electronics.[31]

GPDs can be built exploiting different mechanisms: photo-voltaic (PV),[57,65,66] photo-thermoelectric (PTE),[66–68] photo-gating,[69] plasma-wave assisted[70] and photo-bolometric (PB).[71,72] The dominating effect for a given GPD depends on device configuration, design geometry, and way of operation.[66,73] For telecoms, where high-speed (tens GHz) operation is one of the key requirements,[8,31] PV, PTE, PB are typically considered for waveguide-integrated GPDs,[31] exploiting the ultra-fast (∼fs-ps) carrier dynamics in SLG.[74,75] Early implementations[40–42] of this in Si photonics demonstrated $R_I \sim$ 50-130 mA/W, predominately based on PV, with moderate 3-dB roll-off frequency up to $f_{3\mathrm{dB}} \sim 20$ GHz.[40,41] Building on this, subsequent work either optimised individual performance metrics, e.g. $f_{3\mathrm{dB}} \sim$ 41-76 GHz[44,48] (with $R_I \sim$ 1-7mA/W[44,48]) or R_I ∼0.36-0.37A/W[43,47] ($f_{3\mathrm{dB}} \sim$ 42GHz[47]), or focused on demonstrating integrated GPDs with new waveguide geometries like Si slots[53] ($R_I \sim 0.27$ A/W), platforms like SiN[54] (R_I ∼15mA/W, $f_{3\mathrm{dB}} \sim 30$ GHz), or scalable fabrication.[48] The fasted reported, 110 -128 GHz,[49–51] on-chip GPDs, with R_I ∼0.2-0.5A/W[49–51] are based on PB and PV. However, these device concepts suffer from unavoidable, typically large (∼100μA[51]) dark currents associated with biasing the SLG channel (e.g.∼0.5 V[49,51]).

PTE is ideal for PD operation in a voltage mode, i.e. with direct read-out of the generated photovoltage. In optically illuminated SLG, electron-electron scattering drives the formation of a 'hot' (optically excited)-carrier distribution, described by the Fermi-Dirac function,[76] within <50fs.[74] This can remain at elevated temperatures T_e, well above the lattice temperature T_l, over∼2-4ps time scales,[74] before reaching thermal equilibrium via phonons interaction.[75,77,78] In this hyperthermal state, a photovoltage V_{ph} is generated by a thermo-electric current as for the Seebeck effect,[68] if temperature and chemical potential gradients are present in SLG. The sign and magnitude of V_{ph} depend on the Seebeck coefficient (S), i.e. the proportionality constant between temperature change and photovoltage,[79] and T_{e} profile in SLG:[68]

$$V_{\mathrm{ph}} = \int S(x) \cdot \nabla T_e(x) \, \mathrm{d}x \tag{1}$$

where x is the coordinate along the channel from drain to source, and S is given by:[66–68,79]

$$S(x) = -\frac{\pi^2 k_B^2 T_e}{3e} \frac{1}{\sigma(x)} \frac{\mathrm{d}\sigma(x)}{\mathrm{d}\mu_c} \tag{2}$$

with $\sigma(x)$ the conductivity, k_B the Boltzmann constant, e the electron charge and μ_c the chemical potential ($\mu_c = E_F$ at $T_e = 0$K,[76] with E_F the Fermi energy).

PTE-GPDs have been reported in vertically-illuminated[68,80–83] and waveguide-integrated[45–47] configurations. The latter used SLG flakes prepared by micromechanical cleavage (MC) of graphite,[84] with typical device length of tens of μm,[45–47] achieving external voltage responsivities, defined as $R_V = V_{\mathrm{ph}}/P_{\mathrm{in}}$, up to ~3.5-4.7V/W[45,46] (at zero bias) with speeds $f_{3\mathrm{dB}}$ ~18-65GHz.[45,46] The intrinsic speed limit of PTE-GPDs is related to the cooling time τ_{cooling} of hot electrons in graphene,[31] which is $\sim$ 2-4 ps,[74] thus limiting the photo-switching rate to $\sim 1/\tau_{\mathrm{cooling}}$ = 250-500GHz.[57] Depending on PTE-GPD design configuration and the requirements of the read-out electronics (i.e. output photo-signal to be measured as current or voltage), the responsivity can be characterized in terms of R_I or R_V. The photovoltage generated by the Seebeck effect is associated with a thermoelectric current across the PD by a Ohmic relation[45,46,64,81] $I_{\mathrm{ph}} = V_{\mathrm{ph}}/R$, with R the resistance. When operated at zero source-drain bias to function as photo-generated voltage source, the main contribution to noise in PTE-GPDs comes from thermal (Johnson) noise[83,85] with $v_n = ((4k_BTR)^{\frac{1}{2}}$, where v_n is the root mean square noise voltage per hertz of bandwidth in V Hz$^{-\frac{1}{2}}$. In this case, R becomes a limiting factor for thermal noise and can e.g. be reduced with high-μ SLG and optimised contact resistance.

To increase R_V for PTE-GPDs, Eq.1 suggests two strategies: 1) maximize S; 2) maximize the T_{e} gradient profile in the SLG channel. The former increases with increasing μ (see Methods) and decreasing minimum conductivity σ_{min} due to residual charge carriers. Thus, S can be improved by using high-mobility SLG, e.g. encapsulating SLG in hBN,[86–88] using single-crystals,[88,89] or large (tens μm) domain-sizes,[90] and a transfer processes without

contaminations,[87,91] strain,[91] and cracks.[92] Ref. 31 suggested that $\mu > 10^4$cm^{2}V^{-1}s^{-1} could enable $R_V > 100$V/W. The T_e gradient can be increased by creating a localized heat source[45] generated by enhanced optical absorption in SLG over compact ($< 10\mu$m) device lengths.[50,51] This could be achieved by integrating plasmonic nanostructures.[25,93–97] Sub-wavelength plasmonic confinement and associated enhancement of near-field light-matter interaction were previously used to boost the performance of PDs. E.g., Refs. 93,94 employed plasmonic structures as Schottky contacts to increase R_I in Si-plasmonic PDs. Ref. 25 integrated amorphous Ge with plasmonic slots, reaching internal quantum efficiencies $\sim$ 36% and high-speed operation ∼100 GHz in the O-band. Refs. 98,99 reported microwave detection and mixing based on plasmonic antenna configurations. For PDs based on SLG and other LMs, the incorporation of plasmonic structures was exploited in free-space[95–97] and waveguide-integrated[43,50–52,100] configurations. Refs. 50–52 reported plasmonic enhanced on-chip GPDs based on PV[50,52] and PB[51,52] with $R_I \sim 0.5$ A/W[51] and bandwidth $\sim$ 110GHz[50,51] at 1.55 μm for source-drain bias <1V.

Here, we report compact (∼0.5-4μm), PTE-based, waveguide-integrated, plasmonic-enhanced GPDs for telecom wavelengths with $R_V \sim 12.2$V/W at zero source-drain bias and zero dark current, with a 3dB cutoff frequency∼ 42GHz. To the best of our knowledge, this is the largest R_V to date for waveguide-integrated GPDs operating in voltage mode. We use SLG grown by chemical vapor deposition (CVD) and transferred onto low-loss ($\sim$ 1dB/cm) planarized (i.e. fully-embedded in polished cladding[101]) SiN waveguides with a semi-dry (i.e. combining wet de-lamination from the growth substrate with dry lamination onto the target substrate) transfer,[89] unlike previous PTE GPDs exploiting non-scalable MC SLG.[45,46] Our design relies on Au split-gates to electrostatically create a p-n junction in the SLG channel, as well as to guide a confined SPP waveguide mode. By leveraging optical field enhancement and plasmonic confinement in the gap, we increase light-SLG interaction and optical absorption in the p-n junction region, resulting in a confined electrons heat source, compact device length, and increased R_V. This combines high-performance (large R_V, high-speed, bias-free,

compact, direct V_{ph} read-out) PTE GPDs in the telecom range with scalable fabrication, paving the way for graphene integrated receivers for next-generation transceivers.

The design of our GPD is schematically shown in Fig.1a,b. It comprises a SLG channel on a SiN waveguide supporting a transverse-electric (TE, in-plane) polarized fundamental waveguide mode. Two Au gates are placed above the channel, separated from the SLG by an Al_2O_3 spacer and centrally aligned with respect to the waveguide. When this split-gate structure is DC (direct current) biased, it forms a p-n junction, Fig.1a, and creates a S profile in SLG, as for Eq.2. When an on-chip guided signal reaches the PD area, it is evanescently coupled from the SiN waveguide to the split-gate, which acts as SPP waveguide, Fig.1c. The improvement obtained by using plasmonic guiding with light confinement in the gap (width w_{gap} ~100nm) is: 1) increased strength of electric field and absorption in SLG and 2) shaping the electronic temperature distribution and its gradient in the channel by confining the absorption to the narrow region of the slot. The coupling efficiency, $P_{\mathrm{out}}/P_{\mathrm{in}}$, where P_{out} is the power transferred between two optical components, from photonic to plasmonic waveguide mode can be optimized by tailoring w_{gap} and dielectric spacer thickness (t_{ox}).

To optimize the cross section parameters at λ=1.55μm, we perform optical simulations using a commercial finite difference solver tool (Lumerical MODE). After selecting the fundamental gap plasmon mode for a given design and λ, we extract the optical electric field distribution in the SLG channel to model the absorbed power density that generates the hot carrier distribution as time-averaged electric power dissipation density,[102,103] which we refer to as Joule heat source (J) hereafter. After normalization to an input power of 1μW, this is used in the heat equation:[47,67,80]

$$-\kappa_e(x)\left[\frac{\mathrm{d}^2}{\mathrm{d}x^2}\Delta T_e(x)-\frac{1}{\xi^2}\Delta T_e(x)\right]=J\left(x\right) \tag{3}$$

where $\Delta T_e(x)=T_e(x)-T_l$ is the local temperature fluctuation, ξ is the cooling length (see Methods) and $\kappa_e(x)$ is the electronic thermal conductivity (see Methods). Eq.3 gives the

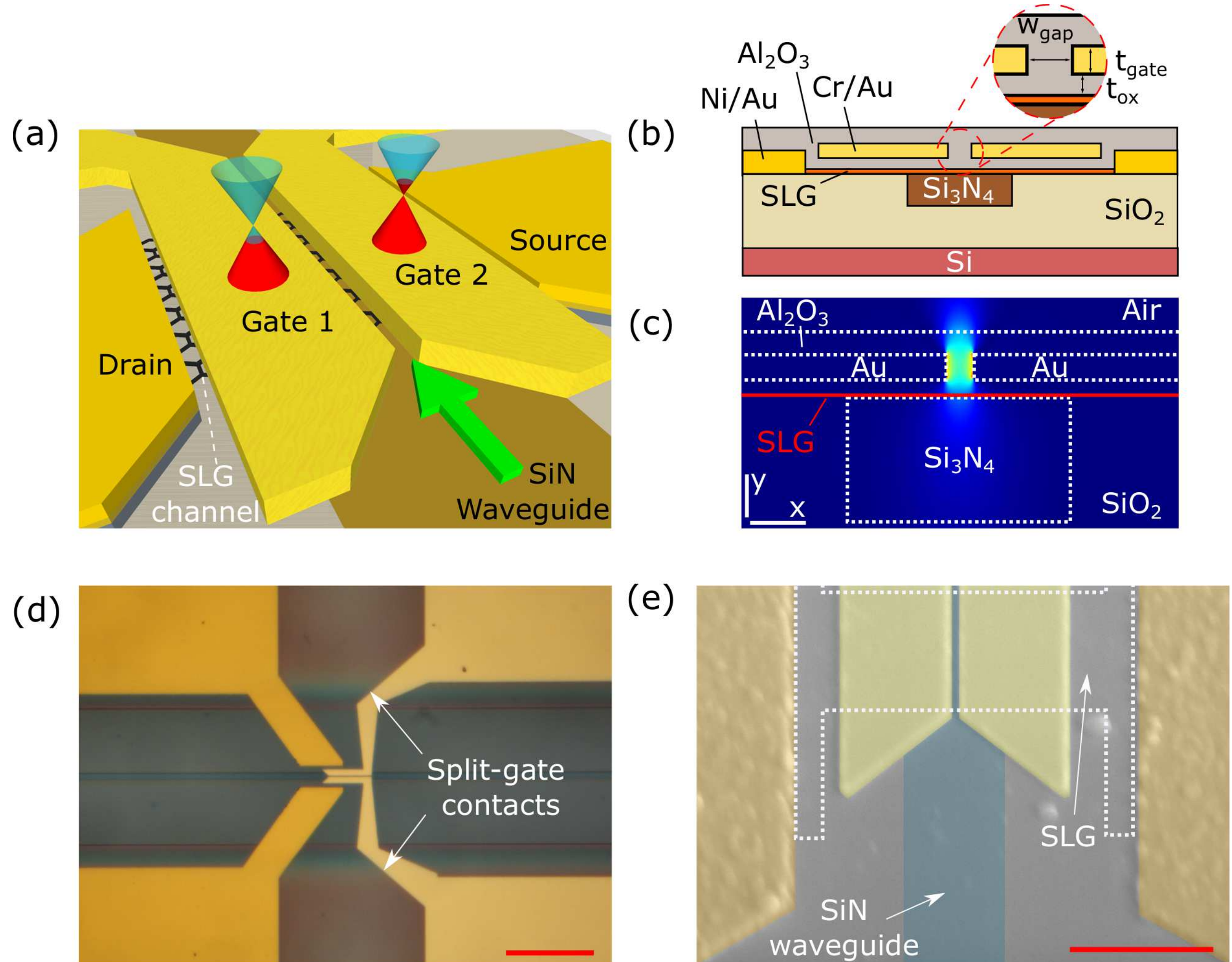

Figure 1: (a) Scheme of our GPD: SLG on SiN waveguide (brown) with split-gates, acting as plasmonic slot waveguide, to create a p-n junction in the channel (as depicted by the Dirac cones above the gates). The green arrow indicates the light propagation direction. (b) Cross-section of the GPD active region. (c) Simulated electric field (E_x, in-plane) distribution of the fundamental SPP waveguide mode. For clarity, only the field component parallel to the SLG channel is shown. The vertical and horizontal scale bars are 100 and 250nm. (d) Optical image of a GPD. Scale bar: 20μm. (e) Scanning electron micrograph of split-gates. False colors: brown, Ni/Au contacts; yellow, Cr/Au gates; green, planarised SiN waveguide; white dashed line, SLG channel. Scale bar: 2μm

$T_e(x)$ profile. Together with the optimum $S(x)$ profile (see Methods), this is used in in Eq.1 to obtain $V_{\rm ph}$. The parameters are chosen to maximize $V_{\rm ph}$. The fabrication process and a more detailed description of the simulations, including coupling between the dielectric and plasmonic waveguides, and the positioning of the SLG channel along the split-gate are presented in Methods. Fig. 1d,e show images of a representative GPD.

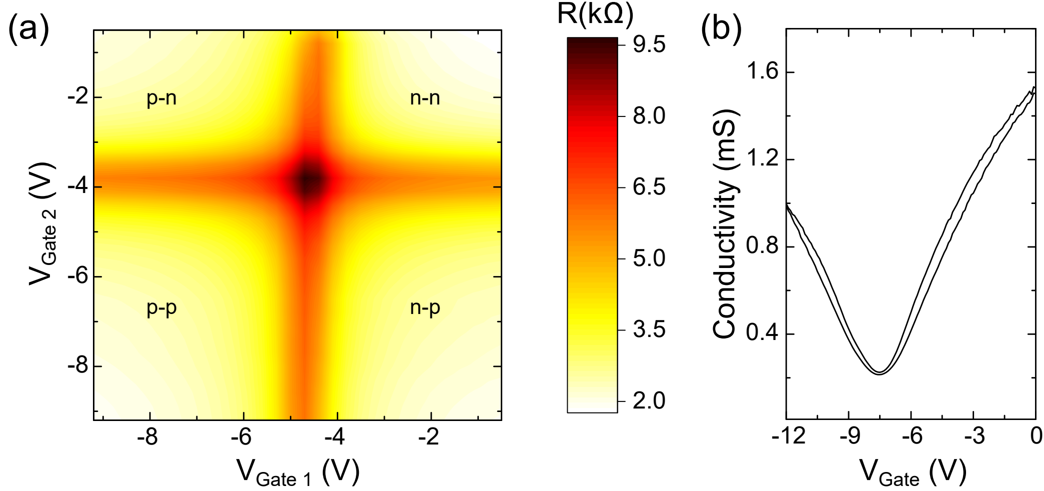

Figure 2: (a) GPD channel resistance as function of split-gate voltages. (b) Conductivity as a function of gate voltage from a 4-terminal measurement on test Hall bars

To determine the operating point of the GPDs, we perform electrical characterizations by sweeping the split-gate voltages ($V_{\rm Gate\ 1}$, $V_{\rm Gate\ 2}$) while measuring the device current I_{DS} under a constant source-drain bias V_{DS}=1mV, using DC probes on micromanipulators and two source measure units. Fig.2a plots the R map of a typical device as a function of $V_{\rm Gate\ 1}$, $V_{\rm Gate\ 2}$. This shows a four-fold pattern, corresponding to the four doping constellations (p-n, n-p, n-n, p-p) for different combinations of gate voltages. The map is symmetric with a maximum R ∼9kΩ at the crossing of the charge neutrality point (CNP), between -4 and -5V. This corresponds to n-doping of the unbiased SLG with n∼7×10^{12}cm^{-2} (∼350meV). R has contributions from channel (R_{ch}) and contact (R_c) resistances. R_{ch} includes a fixed contribution from ungated SLG regions and a gate-dependent one from channel segments underneath the split-gates. The gate-dependent variation in R in Fig.2a suggests R_{ch} as the dominant factor. This is consistent with our contact resistivity (<1kΩμm) for CVD SLG and

the calculated R based on channel geometry and sheet resistance obtained from independent four-terminal measurements on reference Hall bars. From these we also extract an average μ ~2000cm^{2}V^{-1}s^{-1} from linear fits of the conductivity via[104] $\mu = |d\sigma/dV_{\mathrm{Gate}}|/C_{\mathrm{ox}}$, where C_{ox} is the top gate capacitance. Fig.2b is a bi-directional gate sweep of the conductivity, indicating low hysteresis and charge-trapping in the Au/Al_2O_3/SLG gate capacitor.

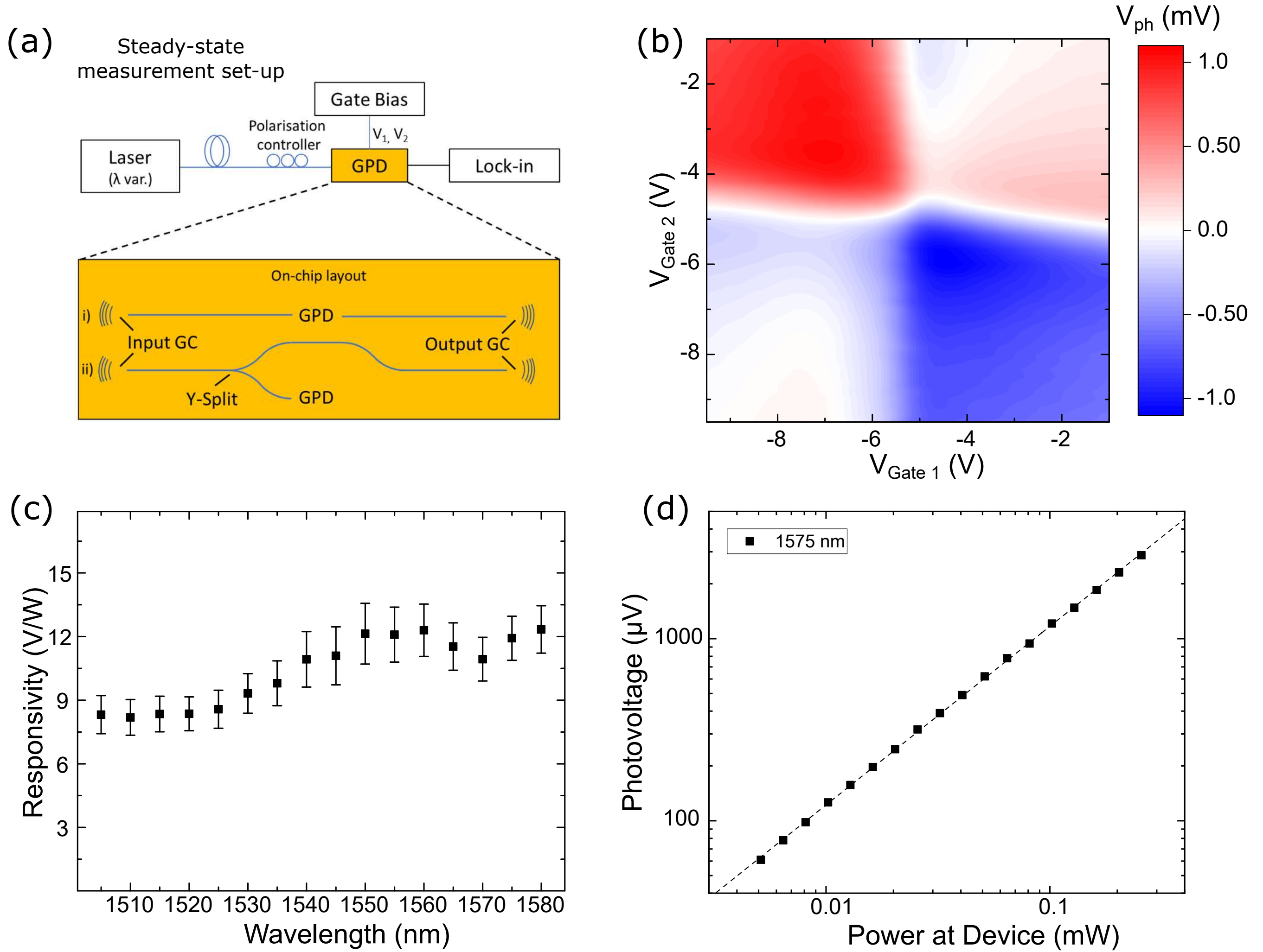

Figure 3: (a) Schematic steady-state photoresponse measurement set-up, including the on-chip lay-out with the passive photonic structure. GPDs are placed on waveguides (i) without or (ii) with 3-dB Y-splits in the lay-out. (b) Experimental photovoltage map for zero bias. (c) Wavelength dependence of responsivity. (d) Power dependence of responsivity at 1575nm.

To record the static photoresponse (see Fig. 3a), we couple continuous wave (CW) transverse-electric (TE, in-plane) polarized light at 1.50-1.58μm into the SiN waveguide

using a single mode optical fibre and an input grating coupler (GC). $V_{\rm ph}$ is recorded between source and drain electrodes across the unbiased (V_{DS}=0V) channel as a function of $V_{\rm Gate\ 1}$ and $V_{\rm Gate\ 2}$, using a lock-in amplifier under internal modulation (square wave, ON-OFF) of the laser at 200 Hz. To ensure constant $P_{\rm in}$ during the experiment, we monitor the transmission with a second fibre positioned over the output GC and connected to an external InGaAs power meter. GPDs are positioned either on bare waveguides ((i) in Fig. 3a) or on one of the branches after a 50-50 Y-split ((ii) in Fig. 3a).

Fig.3b is a $V_{\rm ph}$ map of a typical device at $P_{\rm in} \sim 100\mu$W inside the GPD. The plot exhibits a six-fold pattern with higher response for bipolar (p-n, n-p) junctions and a weaker one with sign-crossing along the diagonal ($V_{\rm Gate\ 1} = V_{\rm Gate\ 2}$) for the unipolar (n-n, p-p) junctions. When the GPD is operated at zero V_{DS}, this indicates a PTE-dominated photodetection as the two sign changes in $V_{\rm ph}$ along a single-gate sweep line (e.g. $V_{\rm Gate\ 2}$ =const.) reflect the two sign changes of the S gradient across the junction, arising from the non-monotonic dependence of S on μ_c[67] (see also Methods). Contributions from PV and PB effects, which can be present in SLG in general,[45,60,66] are negligible or minor here: For PB, because our devices are operated at zero source-drain bias. For PV, because, if this was the main effect, it would result in a two-fold pattern with only one sign-change in $V_{\rm ph}$ along single-gate sweep lines.[67] The measured photoresponse is in good agreement with the calculated one in Fig.8e in Methods. Small asymmetries in the measured photoresponse can stem from fabrication-induced asymmetries in gate geometry, doping variations during PD operation, and non-uniform μ across the graphene p-n junction. We observed a similar behavior on>12 devices of different sizes across 5 chips, the shortest being 500nm in the light propagation direction for a footprint$\sim 3\mu$m^2. For all devices, we got a maximum $V_{\rm ph}$ close to the CNP where S is largest, with a gradual drop-off at higher doping.

To calculate R_V, we first estimate the optical power inside our GPDs by taking into account: a) the combined loss from fiber-to-waveguide coupling and propagation in the Al_2O_3 covered SiN waveguide, from reference measurements on empty waveguides. This combined

loss is wavelength dependent with the spectral response envelope of the GC and e.g. $\sim$ 9.6 dB at the centre wavelength; b) 3dB power reduction from the input laser modulation (square wave, ON-OFF) with a 50% duty cycle; c) 3dB power splitting in the Y-branches and their $\sim$ 0.2dB losses (when applicable). We get $R_V \sim$ 12.2V/W, exceeding the current state-of-the-art[46] by a factor > 2.5, while maintaining scalability with CVD SLG and bias-free operation. The source-drain zero-bias operation in photovoltage mode eliminates noise contribution from the dark current typically observed in PV/ PB GPDs[49–51] and integrated Ge photodiodes.[21,24] Assuming Johnson noise[83,85] as dominant noise source in the absence of applied bias, the measured resistance R and R_V maps give a noise equivalent power,[60,85] NEP $= v_n/R_V$, $\sim$ 600 - 900 pW Hz$^{-\frac{1}{2}}$ in the p-n and n-p regions observed in Fig. 3b. This can be improved by minimizing R (e.g. using higher-mobility SLG, lower contact resistance) and by further maximising R_V (e.g. by improving coupling efficiency and overall absorption in SLG). Reducing R to match the 50Ω of conventional read-out electronics would also lower impedance mismatch and increase the power delivered by the GPDs. The need for this is evident when one translates our measured, record-high R_V for on-chip integrated PTE GPDs to a 50Ω terminated set-up: while the generated photovoltage, as follows from Eq.1, only depends on S and T_e profiles but not on R of channel or external loads, this yields low ($R_V \sim$ 0.2V/W, $R_I \sim$ 4mA/W) values.

Fig.3c plots the R_V wavelength dependence, showing a broadband (1.50-1.58μm) photoresponse covering the C-band (1.53-1.565μm[105]) and beyond. The error bars indicate variations in the wavelength-dependent coupling loss (thus P_{in}), estimated as standard deviation from transmission measurements on >10 reference waveguides. We attribute the gradual increase in R_V with wavelength to a combination of increased overlap between slot mode and SLG and improved coupling efficiency from dielectric to plasmonic waveguide, due to reduced mode mismatch between the fundamental modes in the waveguide and hybrid regions. Fig.3d is the V_{ph} power dependence at 1.575μm for power levels comparable to typical receiver sensitivities required in short-reach optical links.[31] The linear response

indicates a power-independent R_V in the tested P_{in} range, confirming device operation under $|\Delta T_e(x)| \ll T_l$ condition where the electron heat capacity is constant.[64]

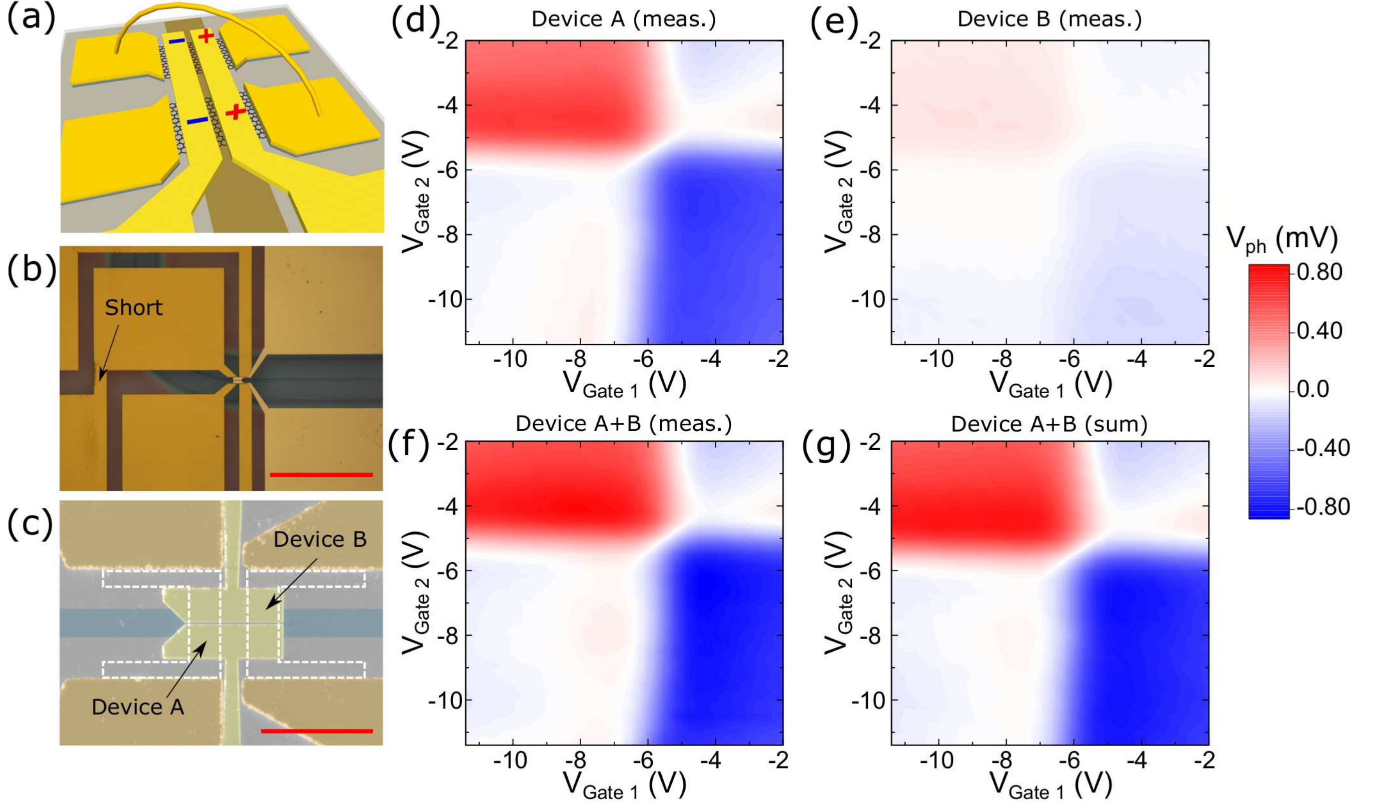

Figure 4: (a) Schematic test structure to measure two GPDs in series. (b) Optical image of contact pad short to connect both GPDs in series. Scale bar: 80μm. (c) SEM image of active region. False colors: brown, Ni/Au contacts; yellow, Cr/Au split gate; green, planarized SiN waveguide. The SLG channels are indicated by white dashed lines. Scale bar: 5μm. (d) Photovoltage map of device A at the start of the SPP waveguide. (e) Photovoltage map of device B at the end of the SPP waveguide. (f) Photovoltage map of devices A, B in series. (g) Sum of A,B photovoltage maps

To highlight our GPDs' behavior as voltage sources, when a signal is generated, we place two devices back to back on the same waveguide and connect them in series. This modified design, Fig.4a, consists of two SLG channels gated from the same split-gate/SPP waveguide. By connecting the drain pad of one channel to the source of the other through a metal lead crossing the waveguide behind the active region of the devices, Fig.4b, we measure both GPDs individually, as well as combined. Fig.4c is a false color SEM of the active region of both detectors. Since each GPD is designed to maximally absorb over the device length, the

power rapidly decays along the propagation direction after the first GPD. We thus place the second device$\sim 1\mu$m from the first.

Figs.4d,e plot the photovoltage maps for both GPDs at $P_{\rm in} \sim 70\mu$W. The GPD closer to the input GC (A) absorbs most of the light and has the six-fold pattern typical of PTE, Fig.4d. The photoresponse of the second GPD (B) is weaker, due to light absorption in SLG and metal, Fig.9d,e. A six-fold pattern is not observed, due to photocurrents generated in the junctions between gated and ungated sections at either end of the SLG channel. Figs.4f,g are photovoltage maps of the combination of both GPDs. The response in series is in Fig.4f, while the sum is in Fig.4g. The two plots are good agreement, confirming that $V_{\rm ph,A+B} = V_{\rm ph,A} + V_{\rm ph,B}$. In order to increase R_V in long (tens μm) PTE-GPDs with absorption only in the SLG channel, one could therefore add the voltages generated in different sections by subdividing the channel into several shorter devices and connecting them as cascaded GPDs. To minimize the metal leads for contacting and connecting individual devices, this configuration could comprise individually gated devices with alternating p-n junctions to form a meandered structure. This would ideally be implemented with transparent gates, such as indium tin oxide, or a second SLG at a distance far enough from the channel, to avoid additional losses. In principle, there is no limit to downscaling individual devices along the waveguide. However, as this would increase R by reducing the width of the SLG channels between drain and source (all the more in a series connections) and therefore harm speed and noise performance, downscaling to sub-micron segments can become impractical in connected configurations.

To evaluate the frequency response we use the optical heterodyne set-up in Fig.5a, combing optical signals at different frequencies. The channel is contacted with an RF probe in G-S configuration. The output of our tunable laser source is combined with a fixed-wavelength laser diode (Thorlabs SFL1550P) and the GPDs' response to the amplitude beating at the difference frequency is monitored with an electrical spectrum analyzer (ESA, Agilent PSX N9030A). The output signal power of each of the two sources is ~ 3 dBm. We combine

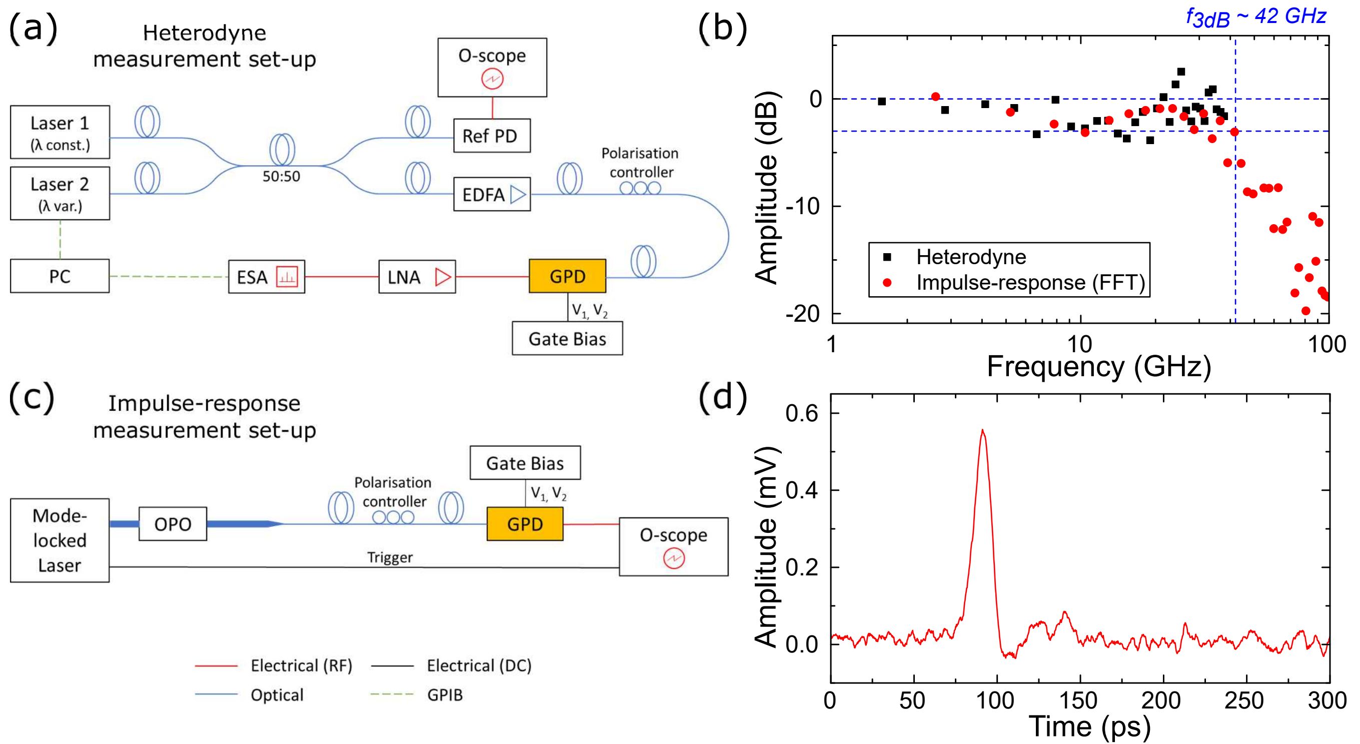

Figure 5: (a) Schematic heterodyne set-up. (b) Frequency response at zero V_{DS} from (black) direct heterodyne measurement and (red) fast Fourier transform of impulse response. (c) Schematic impulse-response set-up. (d) Impulse-response for∼150fs pulses at zero V_{DS} and p-n gate bias

the signals in a 50:50 fibre coupler and, prior to coupling into the SiN waveguide, amplify the combined beating signal up to 15 dBm (∼30mW) using an erbium-doped fibre amplifier (EDFA, Keyopsys CEFA-C-HG) to increase the output signal detected at the ESA. We monitor the signal stability (i.e. output power and position of the difference frequency) using a reference PD and an oscilloscope. To overcome the signal reduction due to impedance mismatch between device R and the 50Ω of the measurement equipment, we use an additional low noise amplifier (LNA) between GPD and ESA. To calibrate our RF set-up prior to measuring the frequency response of our GPD, we independently record the response of LNA and remaining measurement set-up to a low power (-80dBm) input from a 50GHz signal generator.

Fig.5b plots the calibrated response (black squares) to the beating signal at different frequencies, while the split-gate is biased to set an operating point in the p-n junction regime resulting in the largest photoresponse under CW illumination in Fig.3. The response stays within 3dB of the low-frequency (1GHz) reference power until 40GHz, the limit of our measurement set-up.

To determine the cut-off, we therefore modify the set-up (Fig.5c) to perform impulse response measurements, where the response to ultra-short (∼150fs) optical pulses is monitored with an oscilloscope. For excitation, we use the idler of an optical parametric oscillator, pumped by a Ti:Sa mode-locked laser at 1.55μm, attenuated in free-space prior to coupling into the optical fibre. Fig.5d is the measured impulse response at the same operating point as for the heterodyne measurements. We obtain a pulse duration $\Delta t \sim$ 11ps from the full width at half-maximum (FWHM), assuming a Gaussian pulse shape. For Gaussian-shaped pulses, the time-bandwidth product is∼0.44.[106] From this we estimate a $f_{3\text{dB}} \sim 0.44/\Delta t \sim$ 40GHz. The fast Fourier transform of the pulse is in Fig.5b (red circles) after calibration. The trace is in good agreement with the heterodyne response and drops below -3dB at∼ 42GHz. This is consistent with other reports of high-speed MC-SLG-based PTE GPDs, such as the ∼ 42 GHz in Ref. 47, but slower than the highest ∼ 65 GHz of Ref. 45. However, our speed of

f_{3dB} ~42 GHz is the highest reported to date for PTE-based on-chip GPDs made from CVD SLG.

In summary, we reported waveguide-integrated plasmonic enhanced GPDs with an external responsivity~12.2V/W, a -3dB cut-off~42GHz, and small (~3-20μm^2) device footprints, using CVD SLG on SiN. We exploited the integration of an SPP waveguide with a SLG p-n junction to enhance light-SLG interaction and create a confined electron heat-source to obtain a strong, PTE-dominated photoresponse. This paves the way to power-efficient receivers for optoelectronics.

We acknowledge funding from EU Graphene Flagship, ERC Grant Hetero2D, EPSRC Grants EP/K01711X/1, EP/K017144/1, EP/N010345/1, and EP/L016087/1.

Methods

Plasmonic enhanced GPD fabrication

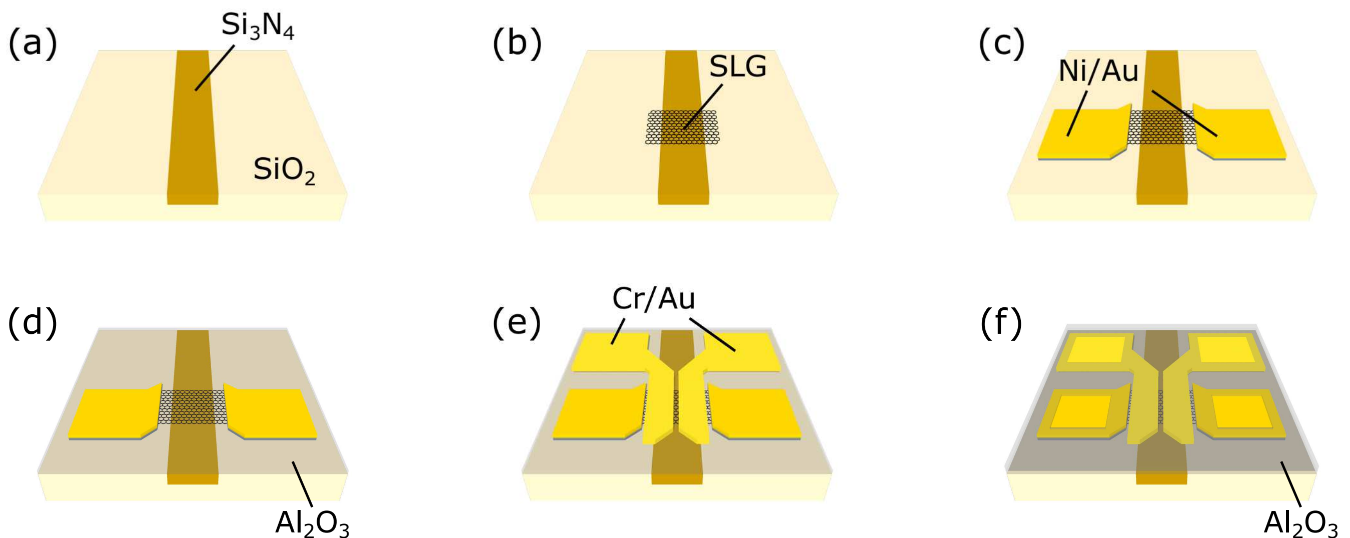

Figure 6: (a) Planarized SiN waveguide. (b) SLG transfer and shaping by oxygen plasma etch. (c) Ni/Au contacts to SLG channel. (d) Al_2O_3 gate oxide deposition. (e) Cr/Au evaporation of split-gate structure. (f) Al_2O_3 encapsulation and contact pads opening

Fig.6 summarizes the fabrication of our GPDs. Planarized SiN waveguides, Fig.6a,

(260nm high, width 0.8-1.5μm) on 15μm SiO_2 are fabricated as follows. The SiN layer is first deposited by low-pressure (LP) CVD. The SiN photonic waveguides are then defined by electron beam lithography (EBL) and reactive ion etching. For surface planarization, a 1.6μm thick boron-phosphorus tetraethyl orthosilicate (BPTEOS) layer is deposited as top cladding and subsequently etched to a final thickness$\sim$ 20nm on top of the SiN waveguides, avoiding chemical mechanical polishing. SLG is grown on pre-patterned, electropolished Cu with Cr nucleation sites as for Ref. 89. After an initial annealing in argon (10mins), SLG growth is initiated at 25mbar with argon, hydrogen, and methane flowing at 900, 100, and 1 standard cubic centimeters per minute (sccm), respectively. After growth, SLG single crystals are placed onto the photonic chips by semi-dry transfer,[89] comprising the spin-coating of a poly(methyl methacrylate) (PMMA) support layer, the attachment of a Kapton frame for handling, electrochemical delamination of SLG in sodium hydroxide, and the lamination onto the target substrate with the help of a micro-manipulator to align the crystals with the photonic structures. After transfer, the PMMA support layer is removed by immersion in acetone and AR600-71 remover. A new PMMA etch mask is then used to shape the device channel and remove excess SLG over grating coupler and waveguides, defined using EBL. This is followed by oxygen plasma etching at 3W, Fig.6b. Next, contacts are defined by another EBL step. Metallization (15nm Ni/40nm Au) is done by sputtering, thermal evaporation and lift-off in acetone, Fig.6c. 30nm Al_2O_3 is used as gate dielectric, via atomic layer deposition (ALD), Fig.6d. An additional EBL step and electron beam evaporation are used to fabricate the plasmonic split gates, Fig.6e. To encapsulate the device and prevent air breakdown in the gap between gate contacts when$\sim$10V is applied, we deposit another 40nm Al_2O_3 by ALD. A laser writer is used to define an etch mask to open access to all contacts, Fig.6f.

The quality of SLG is monitored by Raman spectroscopy at all critical points during the fabrication process, using a Renishaw InVia equipped with a 50x objective (numerical aperture NA=0.75) at 514.5nm with power below 0.5mW to exclude heating effects and risk

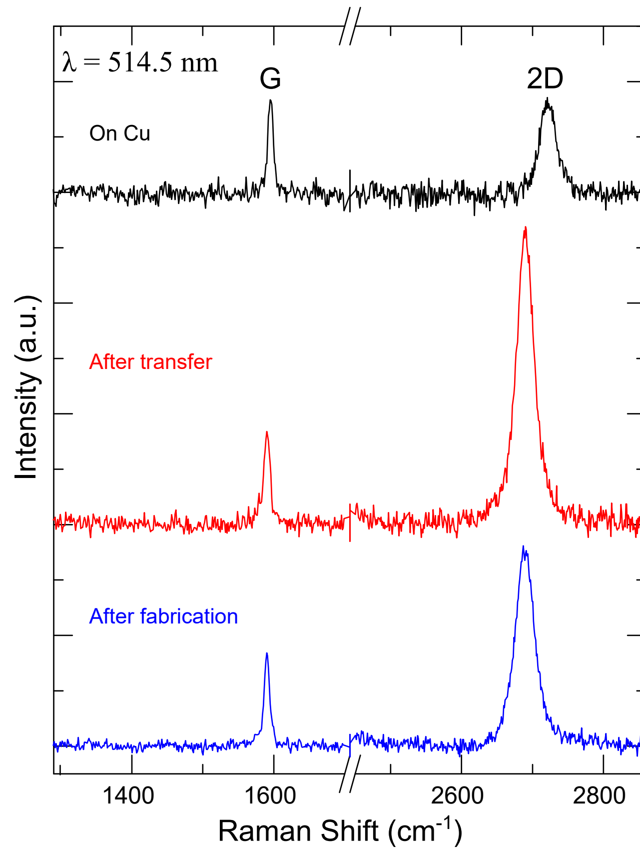

Figure 7: Raman spectra at 514.5 nm for SLG as grown on Cu (black), after transfer onto the SiN waveguide (red), and after device fabrication (blue). All spectra are normalised to the intensity of the G peak, $I(\mathrm{G})$, and are shown after subtraction of the substrate signals.

of damage. Representative spectra of SLG on Cu (after removal of Cu background photoluminescence[107]), after transfer onto the waveguide, and after complete device fabrication, are shown in Fig.7. The absence of a D peak confirms negligible defects are introduced during fabrication. The 2D peaks are single-Lorentzian, confirming the presence of SLG.[108,109] On Cu, the position and FWHM of the G peak are Pos(G)$\sim$1595cm^{-1} and FWHM(G)$\sim$ 8cm^{-1}. The position of the 2D peak, Pos(2D), is$\sim$2721cm^{-1} with FWHM(2D)$\sim$27cm^{-1}. The 2D to G peak intensity, I(2D)/I(G), and area, A(2D)/A(G), ratios are$\sim$ 1 and$\sim$ 3.2. After transfer, Pos(G)$\sim$ 1590cm^{-1}, FWHM(G) $\sim$10cm^{-1}, Pos(2D)$\sim$ 2690cm^{-1}, FWHM(2D)$\sim$28cm^{-1}, I(2D)/I(G) $\sim$ 3.2 and A(2D)/A(G) $\sim$ 8.6. This corresponds to$\sim$ 250meV doping[110,111] and a carrier concentration $\sim$4$\times$10^{12}cm^{-2}. After the final encapsulation, Pos(G)$\sim$ 1590cm^{-1}, FWHM(G)$\sim$ 9cm^{-1}, Pos(2D)$\sim$ 2689cm^{-1}, FWHM(2D)$\sim$ 30cm^{-1}, I(2D)/I(G) $\sim$ 2.2 and A(2D)/A(G) $\sim$ 7.6, indicating a residual $\sim$350meV ($n \sim 7\times10^{12}$cm^{-2}) doping. This additional doping only affects the position of the charge neutrality point and the gate-voltage needed to generate the p-n junctions, since the split-gate structure sets the doping during device operation.

Modelling and simulations

Plasmonic gap width, SLG placement, and thickness of metal and oxide structures are the key parameters to be optimized to achieve maximum photovoltage. To do so, we build a device model in the layout environment of a commercial eigenmode solver (Lumerical MODE Solutions). In order to model SLG in the optical solver and subsequent calculations consistently, we use a volumetric permittivity material model, in which SLG is described as cuboid with finite thickness $t = 0.34$nm and in-plane ($\varepsilon_{\parallel}$) and out-of plane ($\varepsilon_{\perp}$) permittivity are defined as independent tensor elements. To calculate the in-plane relative permittivity for SLG, we use:[112]

$$\varepsilon(\omega) = \varepsilon'(\omega) + i\varepsilon''(\omega) = \varepsilon_r + \frac{i\sigma(\omega)}{\varepsilon_0 \omega t} \tag{4}$$

where $\varepsilon'(\omega)$ and $\varepsilon''(\omega)$ are the real and imaginary part of the relative permittivity $\varepsilon(\omega)$, $\sigma(\omega)$ is the SLG optical conductivity, ω is the angular frequency, ε_r is the background relative permittivity (whose frequency-dependence is ignored in the small 1.5-1.6μm wavelength range under consideration), and ε_0 is the permittivity of free space. $\sigma(\omega)$ is obtained by linear-response[113] in the random-phase approximation,[112] and contains terms describing intraband and interband transitions. While the former can be evaluated analytically,[113] the interband term requires a numerical solution.[112,113] The out-of-plane component of the dielectric tensor matches ε_r.

We then run the eigenmode solver, using the relative permittivity function for SLG, and select the fundamental (gap plasmon) mode (typical propagation losses > 5000 dB/cm)for further processing. We export the simulation mesh grid positions, electric **E** and magnetic **H** data, effective refractive index ($n_{\text{eff}} = \beta/k_0$, where β is the propagation constant of the mode and k_0 is the free space wavevector[114]), and all relevant geometric parameters such as gap and gate width and oxide thickness.

A crucial intermediate step requires the determination of the $T_e(x)$ profile in the SLG channel. The first step establishes the operating regime. As discussed in Refs. 115,116, the energy delivered to the electronic carrier distribution by pumping SLG with a pulsed laser can be sufficiently high to result in $T_e(x) > 1000$K. When modeling photoexcited SLG under these conditions, one has to take into account the $T_e(x)$ dependence[115,116] of all thermodynamic and transport parameters in Eqs.1-3, i.e. μ_c, $\sigma(x)$,$\kappa_e(x)$, resulting in a nonlinear system of coupled equations.

The contrasting case,"weak heating", is characterized by $|\Delta T_e(x)| \ll T_l$.[64,83] Under this condition, Eqs.1-3 can be solved to linear order in the local $T_e(x)$ fluctuation, evaluating all thermodynamic and transport parameters at $T_e(x) = T_l$. A single μ_c is established, following photoexcitation, by electron-electron interactions across the valence and conduction bands, and the thermal conductivity, calculated from the Wiedemann-Franz law $\kappa_e = \pi^2 k_{\text{B}}^2 T_e \sigma/(3e^2)$,[76] is uniform.

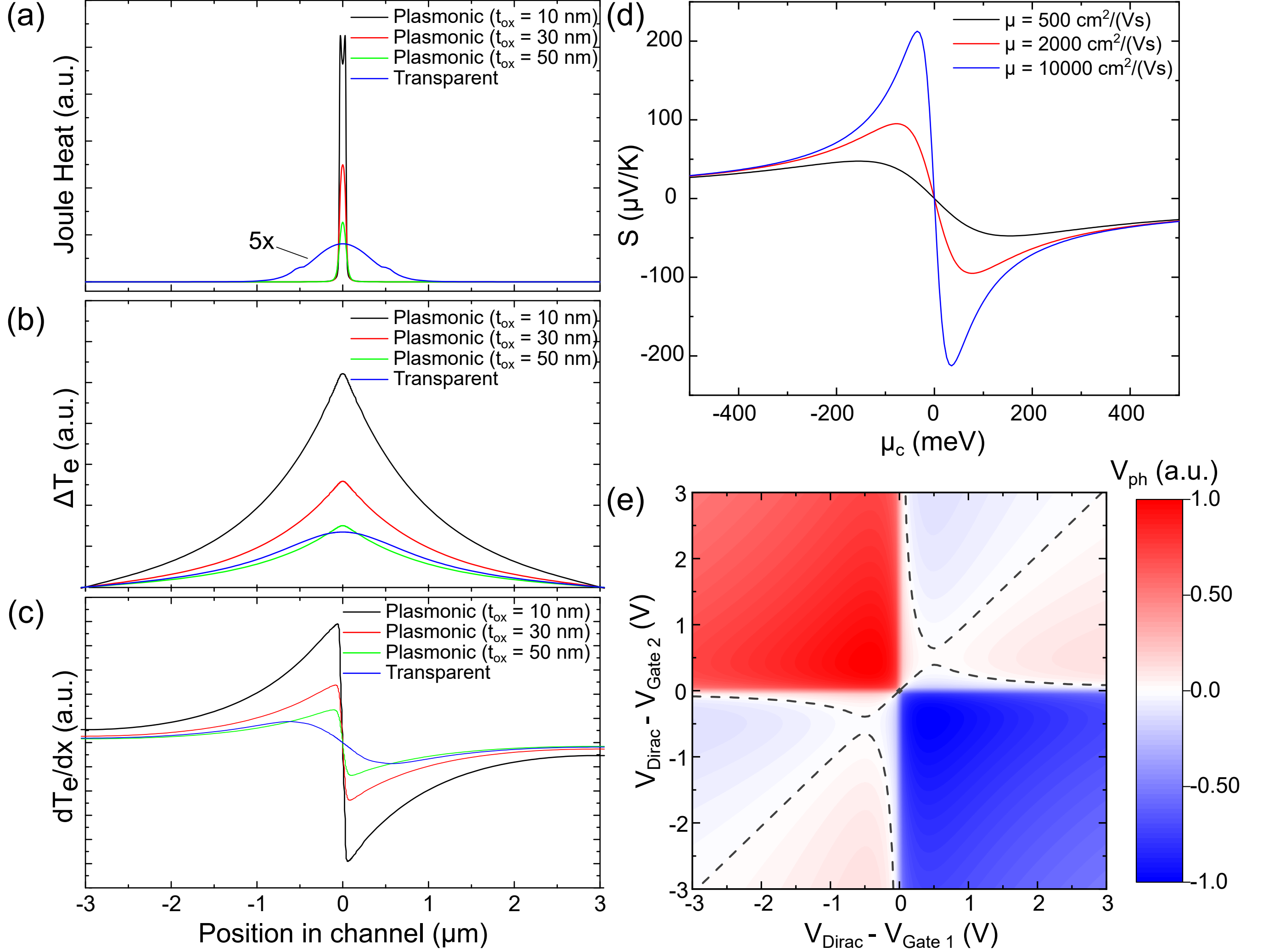

Figure 8: (a) Joule heat source, (b) T_e profile, (c) $\frac{dT_e}{dx}$ across the SLG channel (x-direction) for a representative GPD with plasmonic gates at different heights above the channel compared to gates transparent at 1.55μm. The zero position marks the centre of the channel between source and drain contact. (d) Calculated dependence of Seebeck coefficient on chemical potential for different charge carrier mobilities and constant minimum conductivity. (e) Simulated photovoltage map. $V_{\rm Dirac} - V_{\rm Gate}$ shows the gating relative to the charge neutrality point. The dotted line indicates the zero photovoltage line.

The intended operation of our GPD is under CW or, during data reception, quasi-CW (i.e. the pulse duration exceeds the cooling time of the hot-carrier distribution) illumination with low $P_{\rm in} < 0.1$mW at in-plane incidence. Furthermore, a linear dependence of $V_{\rm ph}$ on $P_{\rm in}$, such as in Fig.3d, is observed.[64] We thus conclude that our device operates in the "weak heating" regime.

In order to evaluate Eq.3, we need to specify the cooling length ξ and the light absorption heat source. In principle, ξ, which describes the energy transfer from the electronic system to the optical phonons,[67] depends on $T_e(x)$ and n. However, in "weak heating", the $T_e(x)$ dependence can be neglected, and n is uniform in the device (with opposite sign in the two regions of the p-n junction) when the photoresponse is maximal. For these reasons, in our calculations, we assume a constant $\xi = 1\mu$m, consistent with experimental values.[47,80] $J(x)$ is calculated from the simulated electric field as the time average of the electric power dissipation density:[102,103]

$$J(x) = \frac{1}{2}\omega\epsilon''|\mathbf{E}|^2 = \frac{1}{2}\frac{\sigma}{t}\mathbf{E}\cdot\mathbf{E}^* \tag{5}$$

To relate $J(x)$ to physically meaningful quantities, we integrate the normal component of the time-averaged Poynting vector over the simulation region and normalize it to a given input power.

After solving Eq.3 for the $T_e(x)$ fluctuation profile $\Delta T_e(x)$, we take its derivative with respect to x and obtain the second factor of the integrand in Eq.1. Figs.8a-c compare the absorption heat source, the resulting $T_e(x)$ profile, and its derivative for a representative GPD in presence of a plasmonic split-gate at different heights over the SLG channel, to an unperturbed fundamental dielectric waveguide mode, where the p-n junction is generated by a transparent (at the chosen λ) gate, such as a split-gate made from a second SLG at a separation large enough to avoid additional optical losses. The beneficial role of plasmonic enhancement, with all other parameters fixed, for a sharper increase in $T_e(x)$ translates to larger $V_{\rm ph}$ if SLG is close to the SPP waveguide (<50nm).

To model S along the channel, we use a Drude conductivity expression,[104] $\sigma = \sigma_{\rm min} + ne\mu$

and $\mu_c = \pm\hbar v_F\sqrt{n\pi}$, where $\hbar$ is the reduced Planck constant and v_F is the Fermi velocity, as discussed in Ref. 55, in Eq.2. This yields:

$$S(\mu, \mu_c) = \frac{2\pi k_B^2 T_e \mu_c}{3\hbar^2 v_F^2} \times \frac{\mu}{\sigma_{\text{min}} + \frac{\mu_c^2 e}{\pi\hbar^2 v_F^2} \times \mu} \tag{6}$$

To highlight the dependence of S on μ and σ_{min} (see Fig. 8d), for fixed μ_c this can be expressed as:

$$S(\mu) = C_1 \times \frac{\mu}{\sigma_{\text{min}} + C_2 \times \mu} \tag{7}$$

where $C_1 = \frac{2\pi k_B^2 T_e \mu_c}{3\hbar^2 v_F^2}$ and $C_2 = \frac{\mu_c^2 e}{\pi\hbar^2 v_F^2}$

We then assume the structure is gated to achieve the maximum S below the gates, as for Eq.2 (opposite in sign but equal in magnitude for the p-n case) and approximate the gap with a linear interpolation between the two. Combining both factors in Eq.1 and computing the integral yields V_{ph} or R_V (if divided by P_{in}) as figure of merit to assess different designs:

$$R_V = \frac{|V_{\text{ph}}|}{P_{\text{in}}} = \frac{1}{P_{\text{in}}}\left| \int S(x)\frac{\mathrm{d}T_e(x)}{\mathrm{d}x}\,\mathrm{d}x \right| \tag{8}$$

To calculate R_V or photovoltage maps as in Fig.8e, we first generate the S profile for all voltage combinations and then proceed via Eqs.8 or 1.

We then perform a sweep of gap width, SLG position, gate oxide thickness, gate contact height as a function of μ in SLG and ε_r. As for Fig.8, shorter distances between SLG channel and SPP waveguide yield larger signals. Furthermore, the SPP waveguide width affects the expected photovoltage in two ways. 1) narrower confinement improves the field strength at the SLG channel and R_V at the cost of higher propagation losses; 2) the ungated SLG at the center of the device with not maximum S shrinks with smaller gaps. The device parameters are then chosen based on these trends, taking into account fabrication complexity, robustness to processing-induced deviations (e.g. suppression of fundamental gap plasmon mode below

a certain gap width), reliability (e.g. oxide break-down) and outcomes of FDTD simulations on coupling and propagation.

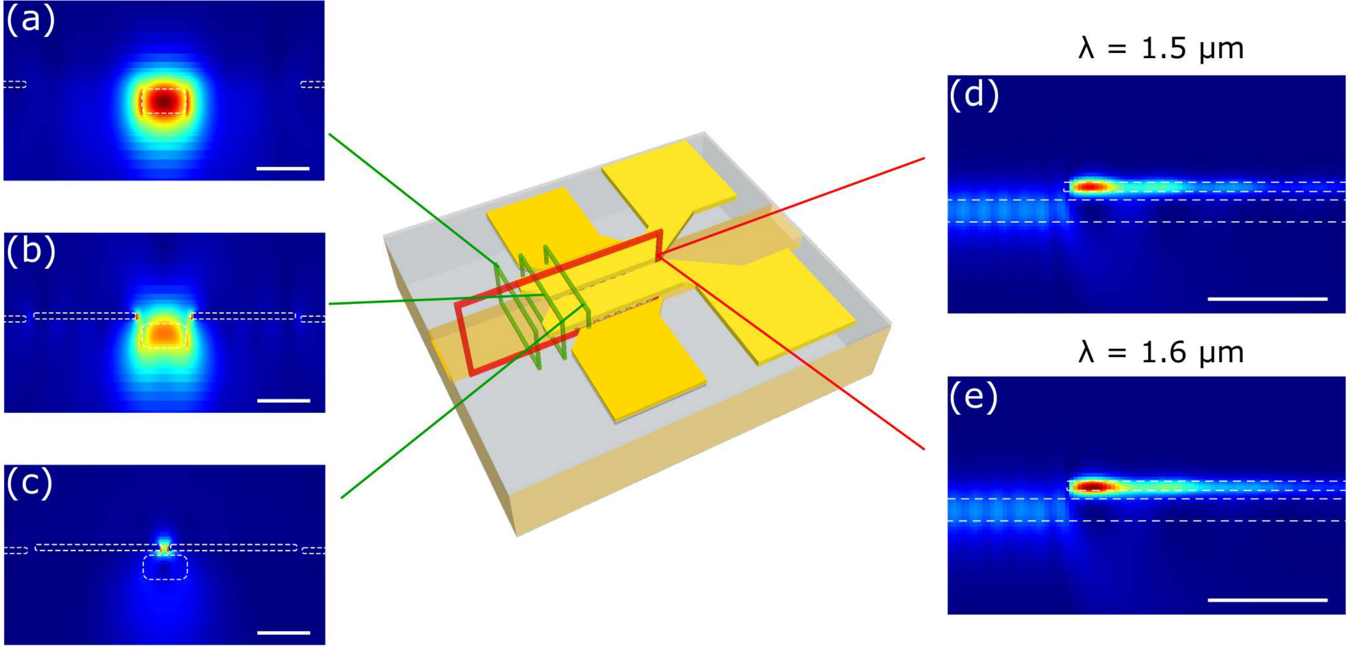

Figure 9: Field distribution (a) before the GPD, (b) during transition, and (c) start of the split-gate/SPP waveguide. Scale bar: 1μm. (d,e) $|\mathbf{E}|^2$ along the center (red box) of dielectric waveguide and GPD at (d)1.5μm and (e) = 1.6μm. Scale bar: 3μm

Extracting **E** and **H** of the fundamental mode in the hybrid region is sufficient for the design of the device cross-section. However, it does not capture the field distribution along the device, since optical losses, transition from dielectric to plasmonic waveguide, and power exchange between different modes that co-exist in the hybrid region remain unaccounted for. We thus perform finite-difference time domain (FDTD) simulations in Lumerical FDTD. We construct a device model in the same way as for the eigenmode analysis and adjust the source settings to 1.5-1.6μm. We launch the fundamental quasi-TE mode of the SiN waveguide towards the GPD and use frequency domain field monitors (FDFM) with various orientations (parallel and perpendicular to the propagation direction) to track the field and power profiles at different points.

Taper-assisted butt-coupling (end-to-end alignment)) is a good option to achieve low ($<$ 0.6dB)[117] insertion loss (IL) for the transition from optical to plasmonic modes. How-

ever, since evanescent coupling (lateral or vertical alignment) provides simpler fabrication[118] and greater flexibility for the placement of devices on top of integrated optical circuits,[119] we use this here despite higher IL. The co-existence of plasmonic and dielectric waveguide leads to oscillating power exchange between both structures.[118–120] For the highest coupling efficiency, the vertical distance between these waveguides is typically$>$ 150nm,[118,119] exploiting interference between quasi-even and quasi-odd eigenmodes.[118–120] In our design, we keep this separation small (tens nm) to ensure overlap between SLG and gap plasmon mode, to avoid a long ($> 5\mu$m) coupling length,[118] and to create a sharper concentration of power close to the front of the plasmonic structure. Within these constraints, the simulated coupling efficiency for this transition is ∼20-40%, depending on w_{gap}, t_{ox}, t_{gate}, as defined in Fig.1, and the dimensions of the underlying Si_3N_4 waveguide. Figs.9a-c plot the field at three cross-sections of a representative GPD. We see transitions from injected mode in dielectric waveguide to field distribution resembling the fundamental gap plasmon.

To obtain the largest R_V, the electric field distribution along the propagation directions needs to be considered. Light absorption in SLG or in the plasmonic structure along the device leads to an exponential decay of optical power.[62] To optimize R_V, a compact ($<$10μm) device with optimized peak absorption and minimal drop-off is preferable. Figs.9d,e display the electric field intensity from a vertical FDMD monitor along the center line of the GPD, at two wavelengths. As expected for this non-adiabatic transition with fast decrease ($<$1μm) of the taper cross-section down to the target gap size, scattering and reflections at the start of the hybrid region reduce the power at the GPD, but the desired sharp intensity profile over length scales that match the fabricated SLG channel widths is achieved. Consequently, we place the SLG channel 100nm after the SPP structure has reached its final gap width. The comparison of field intensities for 1.5 and 1.6μm on the same color scale in Figs.9d,e reveals a larger peak intensity and a longer interaction length for the latter, which indicates improved coupling efficiency at larger λ, as for the wavelength-depended R_V in Fig.3c.

References

(1) *Cisco Visual Networking Index: Forecast and Methodology, 2016 - 2021* (Cisco, 2017). https://www.cisco.com/c/en/us/solutions/collateral/service-provider/visual-networking-index-vni/complete-white-paper-c11-481360.pdf

(2) Andrews, J. G.; Buzzi, S.; Choi, W.; Hanly, S. V.; Lozano, A.; Soong, A. C. K.; Zhang, J. C. *IEEE J. Sel. Areas Commun.* **2014**, 32, 1065-1082.

(3) Osseiran, A.; et al. *IEEE Commun. Mag.* **2014**, 52, 26-35.

(4) Glick, M.; Kimmerling, L. C.; Pfahl, R. C. *Opt. Photonics News* **2018**, 29, 36–41.

(5) Sparks, P. , *The route to a trillion devices - The outlook for IoT investment to 2035* (ARM, 2017). https://community.arm.com/cfs-file/__key/telligent-evolution-components-attachments/01-1996-00-00-00-01-30-09/Arm-_2D00_-The-route-to-a-trillion-devices-_2D00_-June-2017.pdf

(6) Rumley, S.; Nikolova, D.; Hendry, R.; Li, Q.; Calhoun, D.; Bergman, K. *J. Light. Technol.* **2015**, 33, 547-562.

(7) Cheng, Q.; Bahadori, M.; Glick, M.; Rumley, S.; Bergman, K. *Optica* **2018**, 5, 1354–1370.

(8) Thomson, D.; et al. *J. Opt.* **2016**, 18, 073003.

(9) Absil, P. P.; Verheyen, P.; De Heyn, P.; Pantouvaki, M.; Lepage, G.; De Coster, J.; Van Campenhout, J. *Opt. Express* **2015**, 23, 9369–9378.

(10) Atabaki, A. H.; et al. *Nature* **2018**, 556, 349-354.

(11) Subbaraman, H.; Xu, X.; Hosseini, A.; Zhang, X.; Zhang, Y.; Kwong, D.; Chen, R. T. *Opt. Express* **2015**, 23, 2487–2511.

(12) Wooten, E. L.; et al. *IEEE J. Sel. Topics Quantum Electron.* **2000**, 6, 69-82.

(13) Wang, C.; Zhang, M.; Chen, X.; Bertrand, M.; Shams-Ansari, A.; Chandrasekhar, S.; Winzer, P.; Lončar, M. *Nature* **2018**, 562, 101.

(14) Nagarajan, R.; et al. *IEEE J. Sel. Topics Quantum Electron.* **2010**, 16, 1113-1125.

(15) Hosseini, A.; et al. *Opt. Express* **2017**, 25, 18853–18862.

(16) Michel, J.; Liu, J.; Kimerling, L. C. *Nat. Photonics* **2010**, 4, 527–534.

(17) Hawkins, A. R.; Wu, W.; Abraham, P.; Streubel, K.; Bowers, J. E. *Appl. Phys. Lett.* **1997**, 70, 303-305.

(18) Chang, H.; Kuo, Y.; Jones, R.; Barkai, A.; Bowers, J. E. *Opt. Express* **2010**, 18, 23891–23899.

(19) Chrostowski, L.; Hochberg, M. *Silicon Photonics Design: From Devices to Systems*, Cambridge University Press: Glasgow, 2015.

(20) Vivien, L.; Osmond, J.; Fédéli, J.; Marris-Morini, D.; Crozat, P.; Damlencourt, J.; Cassan, E.; Lecunff, Y.; Laval, S. *Opt. Express* **2009**, 17, 6252–6257.

(21) DeRose, C. T.; Trotter, D. C.; Zortman, W. A.; Starbuck, A. L.; Fisher, M.; Watts, M. R.; Davids, P. S. *Opt. Express* **2011**, 19, 24897–24904.

(22) Vivien, L.; Polzer, A.; Marris-Morini, D.; Osmond, J.; Hartmann, J. M.; Crozat, P.; Cassan, E.; Kopp, C.; Zimmermann, H.; Fédéli, J. M. *Opt. Express* **2012**, 20, 1096–1101.

(23) Novack, A.; et al. *Opt. Express* **2013**, 21, 28387–28393.

(24) Chen, H.; Verheyen, P.; De Heyn, P.; Lepage, G.; De Coster, J.; Balakrishnan, S.; Yao, W.; Shen, L.; Roelkens, G.; Van Campenhout, J. *Opt. Express* **2016**, 24, 4622–4631.

(25) Salamin, Y.; Ma, P.; Baeuerle, B.; Emboras, A.; Fedoryshyn, Y.; Heni, W.; Cheng, B.; Josten, A.; Leuthold, J. *ACS Photonics* **2018**, 5, 3291–3297.

(26) Wang, J.; Lee, S. *Sensors* **2011**, 11, 696–718.

(27) Ye, H.; Yu, J. *Sci. Technol. Adv. Mater.* **2014**, 15, 024601.

(28) Sorianello, V.; De Iacovo, A.; Colace, L.; Fabbri, A.; Tortora, L.; Buffagni, E.; Assanto, G. *Appl. Phys. Lett.* **2012**, 101, 081101.

(29) Liu, J.; Cannon, D. D.; Wada, K.; Ishikawa, Y.; Jongthammanurak, S.; Danielson, D. T.; Michel, J.; Kimerling, L. C. *Appl. Phys. Lett.* **2005**, 87, 011110.

(30) Rahim, A.; et al. *J. Lightwave Technol.* **2017**, 35, 639–649.

(31) Romagnoli, M.; Sorianello, V.; Midrio, M.; Koppens, F. H. L.; Huyghebaert, C.; Neumaier, D.; Galli, P.; Templ, W.; D'Errico, A.; Ferrari, A. C. *Nat. Rev. Mater.* **2018**, 3, 392–414.

(32) Liu, M.; Yin, X.; Ulin-Avila, E.; Geng, B.; Zentgraf, T.; Ju, L.; Wang, F.; Zhang, X. *Nature* **2011**, 474, 64–67.

(33) Liu, M.; Yin, X.; Zhang, X. *Nano Lett.* **2012**, 12, 1482–1485.

(34) Hu, Y.; Pantouvaki, M.; Van Campenhout, J.; Brems, S.; Asselberghs, I.; Huyghebaert, C.; Absil, P.; Van Thourhout, D. *Laser Photon. Rev.* **2016**, 10, 307–316.

(35) Phare, C. T.; Daniel Lee, Y.; Cardenas, J.; Lipson, M. *Nat. Photonics* **2015**, 9, 511–514.

(36) Sorianello, V.; Midrio, M.; Romagnoli, M. *Opt. Express* **2015**, 23, 6478–6490.

(37) Sorianello, V.; Midrio, M.; Contestabile, G.; Asselberghs, I.; Van Campenhout, J.; Huyghebaert, C.; Goykhman, I.; Ott, A. K.; Ferrari, A. C.; Romagnoli, M. *Nat. Photonics* **2018**, 12, 40–44.

(38) Giambra, M. A.; Sorianello, V.; Miseikis, V.; Marconi, S.; Montanaro, A.; Galli, P.; Pezzini, S.; Coletti, C.; Romagnoli, M. *Opt. Express* **2019**, 27, 20145–20155.

(39) Sun, Z.; Martinez, A.; Wang, F. *Nat. Photonics* **2016**, 10, 227–238.

(40) Gan, X.; Shiue, R.; Gao, Y.; Meric, I.; Heinz, T. F.; Shepard, K.; Hone, J.; Assefa, S.; Englund, D. *Nat. Photonics* **2013**, 7, 883–887.

(41) Pospischil, A.; Humer, M.; Furchi, M. M.; Bachmann, D.; Guider, R.; Fromherz, T.; Mueller, T. *Nat. Photonics* **2013**, 7, 892–896.

(42) Wang, X.; Cheng, Z.; Xu, K.; Tsang, H. K.; Xu, J. *Nat. Photonics* **2013**, 7, 888–891.

(43) Goykhman, I.; et al. *Nano Lett.* **2016**, 16, 3005-3013.

(44) Schall, D.; et al. *ACS Photonics* **2014**, 1, 781–784.

(45) Schuler, S.; Schall, D.; Neumaier, D.; Dobusch, L.; Bethge, O.; Schwarz, B.; Krall, M.; Mueller, T. *Nano Lett.* **2016**, 16, 7107-7112.

(46) Schuler, S.; Schall, D.; Neumaier, D.; Schwarz, B.; Watanabe, K.; Taniguchi, T.; Mueller, T. *ACS Photonics* **2018**, 5, 4758-4763.

(47) Shiue, R. J.; Gao, Y.; Wang, Y.; Peng, C.; Robertson, A. D.; Efetov, D. K.; Assefa, S.; Koppens, F. H. L.; Hone, J.; Englund, D. *Nano Lett.* **2015**, 15, 7288–7293.

(48) Schall, D.; Porschatis, C.; Otto, M.; Neumaier, D. *J. Phys. D: Appl. Phys.* **2017**, 50, 124004.

(49) Schall, D.; Pallecchi, E.; Ducournau, G.; Avramovic, V.; Otto, M.; Neumaier, D. , in *Optical Fiber Communication Conference*, M2I.4, (Optical Society of America,2018).

(50) Ding, Y.; Cheng, Z.; Zhu, X.; Yvind, K.; Dong, J.; Galili, M.; Hu, H.; Mortensen, N. A.; Xiao, S.; Oxenløwe, L. K. , *arXiv*, 1808.04815 (2018).

(51) Ma, P.; Salamin, Y.; Baeuerle, B.; Josten, A.; Heni, W.; Emboras, A.; Leuthold, J. *ACS Photonics* **2019**, 6, 154–161.

(52) Ma, Z.; Kikunage, K.; Wang, H.; Sun, S.; Amin, R.; Tahersima, M.; Maiti, R.; Miscuglio, M.; Dalir, H.; Sorger, V. J. , *arXiv*, 1812.00894 (2018).

(53) Wang, J.; Cheng, Z.; Chen, Z.; Wan, X.; Zhu, B.; Tsang, H. K.; Shu, C.; Xu, J. *Nanoscale* **2016**, 8, 13206–13211.

(54) Gao, Y.; Zhou, G.; Zhao, N.; Tsang, H. K.; Shu, C. *Opt. Lett.* **2018**, 43, 1399–1402.

(55) Bonaccorso, F.; Sun, Z.; Hasan, T.; Ferrari, A. C. *Nat. Photonics* **2010**, 4, 611–622.

(56) Urich, A.; Unterrainer, K.; Mueller, T. *Nano Lett.* **2011**, 11, 2804–2808.

(57) Xia, F.; Mueller, T.; Lin, Y.; Valdes-Garcia, A.; Avouris, P. *Nat. Nanotechnol.* **2009**, 4, 839–843.

(58) Nair, R. R.; Blake, P.; Grigorenko, A. N.; Novoselov, K. S.; Booth, T. J.; Stauber, T.; Peres, N. M. R.; Geim, A. K. *Science* **2008**, 320, 1308–1308.

(59) Dawlaty, J. M.; Shivaraman, S.; Strait, J.; George, P.; Chandrashekhar, M.; Rana, F.; Spencer, M. G.; Veksler, D.; Chen, Y. *Appl. Phys. Lett.* **2008**, 93, 131905.

(60) Koppens, F. H.; Mueller, T.; Avouris, P.; Ferrari, A. C.; Vitiello, M. S.; Polini, M. *Nat. Nanotechnol.* **2014**, 9, 780–793.

(61) Goossens, S.; et al. *Nat. Photonics* **2017**, 11, 366–371.

(62) Youngblood, N.; Li, M. *Nanophotonics* **2017**, 6, 1205–1218.

(63) Liu, M.; Zhang, X. *Nat. Photonics* **2013**, 7, 851–852.

(64) Tielrooij, K.; et al. *Nat. Nanotechnol.* **2015**, 10, 437–443.

(65) Mueller, T.; Xia, F.; Avouris, P. *Nat. Photonics* **2010**, 4, 297–301.

(66) Echtermeyer, T. J.; et al. *Nano Lett.* **2014**, 14, 3733-3742.

(67) Song, J. C. W.; Rudner, M. S.; Marcus, C. M.; Levitov, L. S. *Nano Lett.* **2011**, 11, 4688–4692.

(68) Gabor, N. M.; Song, J. C.; Ma, Q.; Nair, N. L.; Taychatanapat, T.; Watanabe, K.; Taniguchi, T.; Levitov, L. S.; Jarillo-Herrero, P. *Science* **2011**, 334, 648–652.

(69) Konstantatos, G.; Badioli, M.; Gaudreau, L.; Osmond, J.; Bernechea, M.; de Arquer, F. P. G.; Gatti, F.; Koppens, F. H. L. *Nat. Nanotechnol.* **2012**, 7, 363–368.

(70) Vicarelli, L.; Vitiello, M. S.; Coquillat, D.; Lombardo, A.; Ferrari, A. C.; Knap, W.; Polini, M.; Pellegrini, V.; Tredicucci, A. *Nat. Mater.* **2012**, 11, 865–871.

(71) Freitag, M.; Low, T.; Xia, F.; Avouris, P. *Nat. Photonics* **2013**, 7, 53-59.

(72) Sassi, U.; et al. *Nat. Commun.* **2017**, 8, 14311.

(73) Huo, N.; Konstantatos, G. *Adv. Mater.* **2018**, 30, 1801164.

(74) Brida, D.; et al. *Nat. Commun.* **2013**, 4, 1987.

(75) Tomadin, A.; Brida, D.; Cerullo, G.; Ferrari, A. C.; Polini, M. *Phys. Rev. B* **2013**, 88, 035430.

(76) Kittel, C. *Introduction to solid state physics*, Wiley New York: New York, 1996.

(77) Bonini, N.; Lazzeri, M.; Marzari, N.; Mauri, F. *Phys. Rev. Lett.* **2007**, 99, 176802.

(78) Lazzeri, M.; Piscanec, S.; Mauri, F.; Ferrari, A.; Robertson, J. *Phys. Rev. Lett.* **2005**, 95, 236802.

(79) Ashcroft, N.; Mermin, N. *Solid State Physics*, Harcourt College Publishers: Fort Worth, 1976.

(80) Ma, Q.; Gabor, N. M.; Andersen, T. I.; Nair, N. L.; Watanabe, K.; Taniguchi, T.; Jarillo-Herrero, P. *Phys. Rev. Lett.* **2014**, 112, 247401.

(81) Freitag, M.; Low, T.; Avouris, P. *Nano Lett.* **2013**, 13, 1644–1648.

(82) Herring, P. K.; Hsu, A. L.; Gabor, N. M.; Shin, Y. C.; Kong, J.; Palacios, T.; Jarillo-Herrero, P. *Nano Lett.* **2014**, 14, 901–907.

(83) Castilla, S.; et al. *Nano Lett.* **2019**, 19, 2765–2773.

(84) Novoselov, K. S.; Jiang, D.; Schedin, F.; Booth, T. J.; Khotkevich, V. V.; Morozov, S. V.; Geim, A. K. *Proc. Natl. Acad. Sci. U.S.A.* **2005**, 102, 10451–10453.

(85) Fang, Y.; Armin, A.; Meredith, P.; Huang, J. *Nat. Photonics* **2019**, 13, 1–4.

(86) Wang, L.; et al. *Science* **2013**, 342, 614–7.

(87) Purdie, D. G.; Pugno, N. M.; Taniguchi, T.; Watanabe, K.; Ferrari, A. C.; Lombardo, A. *Nat. Commun.* **2018**, 9, 5387.

(88) De Fazio, D.; et al., *arXiv*, 1904.01405 (2019).

(89) Miseikis, V.; Bianco, F.; David, J.; Gemmi, M.; Pellegrini, V.; Romagnoli, M.; Coletti, C. *2D Mater.* **2017**, 4, 021004.

(90) Li, X.; et al. *Nano Lett.* **2010**, 10, 4328–4334.

(91) Wang, B.; Huang, M.; Tao, L.; Lee, S. H.; Jang, A.; Li, B.; Shin, H. S.; Akinwande, D.; Ruoff, R. S. *ACS Nano* **2016**, 10, 1404–1410.

(92) Suk, J. W.; Kitt, A.; Magnuson, C. W.; Hao, Y.; Ahmed, S.; An, J.; Swan, A. K.; Goldberg, B. B.; Ruoff, R. S. *ACS Nano* **2011**, 5, 6916–6924.

(93) Goykhman, I.; Desiatov, B.; Khurgin, J.; Shappir, J.; Levy, U. *Nano Lett.* **2011**, 11, 2219–2224.

(94) Goykhman, I.; Desiatov, B.; Khurgin, J.; Shappir, J.; Levy, U. *Opt. Express* **2012**, 20, 28594–28602.

(95) Echtermeyer, T. J.; Britnell, L.; Jasnos, P. K.; Lombardo, A.; Gorbachev, R. V.; Grigorenko, A. N.; Geim, A. K.; Ferrari, A. C.; Novoselov, K. S. *Nat. Commun.* **2011**, 2, 455–458.

(96) Fang, Z.; Liu, Z.; Wang, Y.; Ajayan, P. M.; Nordlander, P.; Halas, N. J. *Nano Lett.* **2012**, 12, 3808–3813.

(97) Echtermeyer, T. J.; Milana, S.; Sassi, U.; Eiden, A.; Wu, M.; Lidorikis, E.; Ferrari, A. C. *Nano Lett.* **2016**, 16, 8–20.

(98) Salamin, Y.; et al. *Nano Lett.* **2015**, 15, 8342–8346.

(99) Salamin, Y.; et al. *Nat. Photonics* **2018**, 12, 749–753.

(100) Chen, C.; Youngblood, N.; Peng, R.; Yoo, D.; Mohr, D. A.; Johnson, T. W.; Oh, S.; Li, M. *Nano Lett.* **2017**, 17, 985–991.

(101) Reed, G. T. *Silicon Photonics: The State of the Art*, John Wiley & Sons: Chichester, 2008.

(102) Desiatov, B.; Goykhman, I.; Levy, U. *Nano Lett.* **2014**, 14, 648–652.

(103) Shin, W.; Raman, A.; Fan, S. *J. Opt. Soc. Am. B* **2012**, 29, 1048–1054.

(104) Novoselov, K. S.; Geim, A. K.; Morozov, S. V.; Jiang, D.; Zhang, Y.; Dubonos, S. V.; Grigorieva, I. V.; Firsov, A. A. *Science* **2004**, 306, 666–669.

(105) Senior, J. M.; Jamro, M. Y. *Optical fiber communications: principles and practice*, Pearson Education: Harlow, 2009.

(106) Diels, J.; Rudolph, W. *Ultrashort laser pulse phenomena*, Elsevier: London, 2006.

(107) Lagatsky, A.; et al. *Appl. Phys. Lett.* **2013**, 102, 013113.

(108) Ferrari, A. C.; et al. *Phys. Rev. Lett.* **2006**, 97, 187401.

(109) Ferrari, A. C.; Basko, D. M. *Nat. Nanotechnol.* **2013**, 8, 235–246.

(110) Das, A.; et al. *Nat. Nanotechnol.* **2008**, 3, 210–215.

(111) Basko, D. M.; Piscanec, S.; Ferrari, A. C. *Phys. Rev. B* **2009**, 80, 165413.

(112) Emani, N. K.; Kildishev, A. V.; Shalaev, V. M.; Boltasseva, A. *Nanophotonics* **2015**, 4, 214–223.

(113) Hanson, G. W. *J. Appl. Phys.* **2008**, 103, 064302. *ibid.* **2013**, 113, 029902.

(114) Reed, G. T.; Knights, A. P. *Silicon Photonics: An Introduction*, John Wiley & Sons: Chichester, 2004.

(115) Soavi, G.; et al. *Nat. Nanotechnol.* **2018**, 13, 583-588.

(116) Soavi, G.; et al., *arXiv*, 1903.00989 (2019).

(117) Tian, J.; Yu, S.; Yan, W.; Qiu, M. *Appl. Phys. Lett.* **2009**, 95, 013504.

(118) Dabos, G.; et al. *IEEE Photon. J.* **2018**, 10, 2700308.

(119) Li, Q.; Qiu, M. *Opt. Express* **2010**, 18, 15531–15543.

(120) Delacour, C.; Blaize, S.; Grosse, P.; Fedeli, J. M.; Bruyant, A.; Salas-Montiel, R.; Lerondel, G.; Chelnokov, A. *Nano Lett.* **2010**, 10, 2922–2926.